Nanoscale

COMMUNICATION

View Article Online
View Journal

Cite this: DOI: 10.1039/c9nr00901a

Received 28th January 2019,
Accepted 20th March 2019

DOI: 10.1039/c9nr00901a

rsc.li/nanoscale

Plasmonic heating induced by Au nanoparticles for quasi-ballistic thermal transport in multi-walled carbon nanotubes†

Yanru Xu,‡[a] Xiaoguang Zhao,‡[b] Aobo Li,[b] Yanan Yue,*[a,b] Jin Jiang[a] and Xin Zhang *[b]

The plasmon resonances of nanostructures enable wide applications from highly sensitive sensing to high-resolution imaging, through the improvement of photogeneration rate stimulated by the local field enhancement. However, quantitative experimental studies on the localized heating and the thermal transport process in the vicinity of plasmonics are still lacking because of the diffraction limit in conventional optothermal methodologies. In this work, we demonstrate an approach based on Raman thermometry to probe the near-field heating caused by plasmonics. An array of Au nanoparticles (AuNPs) fabricated by the template-assisted method is used to generate the near field effect. Multi-walled carbon nanotubes (MWCNTs) dispersed on the AuNPs are employed to quantify the near-field heating from their Raman peak shifts. Results show that the temperature rise in MWCNTs on AuNPs is much higher than that in a control group under the same laser irradiation. Further analysis indicates that the enhanced photon absorption of MWCNTs attributed to plasmon resonances is partially responsible for the different heating effect. The nonuniform thermal hot spots at the nanoscale can result in the quasi-ballistic thermal transport of phonons in MWCNTs, which is another reason for the temperature rise. Our results can be used to understand plasmonic heating effects as well as to explore quasi-ballistic thermal transport in carbon-based low-dimensional materials by tailoring the geometry or size of plasmonic nanostructures.

Introduction

Plasmon resonances of nanostructures excited by laser irradiation exhibit extraordinary local field enhancement, and are extensively used to improve the photogeneration rate of optical processes, enabling a wide range of applications ranging from highly sensitive sensing to high-resolution imaging.[1–3] Simultaneously, the confined electromagnetic field around the plasmonic structure also induces significant light absorption and manifests heating in the surrounding medium, which evolves into plenty of applications.[4] For example, the enhanced optical field of metallic nanoantennas in a heat-assisted magnetic recording (HAMR) system can be used to heat the medium to hundreds of degrees Celsius for efficient magnetic writing.[5] Besides, the plasmonic heating effect *via* the damping of plasmon oscillation promises a variety of novel applications including photo-induced water vaporization,[6,7] photon energy conversion,[8,9] visible-light photocatalysis[9,10] and laser nanofabrication.[11] The quantitative study of the thermophysical properties is essential for the exploration and utilization of the localized heating effect.

Theoretical calculations and numerical simulations have been conducted to study the plasmonic heating of nanostructures.[12–14] Gold-based nanoparticles (AuNPs),[15] nanostars,[16] and nanowires[17] have been shown to exhibit the plasmonic heating effect in many numerical studies. The titanium nitride (TiN) and zirconium nitride (ZrN) NPs are also ideal candidates for HAMR, because of their stability at high temperatures.[18] An array of AuNPs on a substrate advances in causing localized nanoscale heating compared with those dispersed in solutions.[19] A diabolo antenna is more favorable for nanoscale heat generation compared with bow-tie structures.[20] The incorporation of the antenna into a plasmonic lens has been demonstrated to act as a complementary structure for yielding five times more enhanced thermal hot spots.[20] The nano-gap between the gold tips and the substrate could lead to a temperature rise three orders of magnitude higher than that of the substrate without the tips.[21] Besides, the near-field heating of the tip-substrate cavity may bring material deformation to the substrate.[22] To manage and explore the plasmonic heating, especially for structures at nanoscale, experimental validation is needed for understanding and then controlling the plasmonic heating and nanoscale heat generation.

[a]*Key Laboratory of Hydraulic Machinery Transients (MOE), School of Power and Mechanical Engineering, Wuhan University, Wuhan, Hubei 430072, China. E-mail: yyue@whu.edu.cn*

[b]*Department of Mechanical Engineering, Boston University, Boston, Massachusetts 02215, USA. E-mail: xinz@bu.edu*

†Electronic supplementary information (ESI) available. See DOI: 10.1039/c9nr00901a

‡These authors contributed equally.

Experimental works on nanoscale heat generation due to the plasmonic heating effect are not as many as simulations since the thermal characterization is challenging due to the intrinsic property of measurement principles. The conventional optical techniques such as infrared thermometry are limited by the diffraction effect of light. The accurate characterizations of localized temperature and plasmonic heat intensity are difficult but critical. Previously, the bolometric approach,[17] photoluminescence approach[20] and plasmonic absorption band[23] have been employed in thermal characterizations of gold nanostructures, while suffering from the uncertainties induced by material emissivity, intensity fluctuation or the complex calibration process. The development of novel thermometry techniques at nanoscale is very much in demand for understanding the thermophysical processes under plasmonics effect. Strong photogeneration from plasmonic structures also yield Raman enhancement, known as surface-enhanced Raman scattering. For a decade, Raman spectroscopy has been used as a powerful tool for the thermal characterization of carbon-based low-dimensional materials, such as carbon nanotubes (CNTs)[24–26] and graphene.[27–29] The resolution of Raman thermometry mainly depends on the size of the probed materials or the laser spot. If the size of the target material is smaller than the laser spot size, and there is only one sample within the spot, Raman thermometry is capable of characterizing the thermal properties of such a structure.[30] Thus, it could break the diffraction limit from this point of view.

With the advanced miniaturization and increased power density of electronic devices, the excessive heat has to be removed to reduce the local high temperature induced by hotspots for safe and reliable operations.[31] CNTs provide an promising opportunity for thermal management, which can be used as the one-dimensional heat spreader connecting the hotspot and the heat sinks.[32] As high-thermal-conductivity nanomaterials, CNTs are promising in next-generation electronic applications. Temperature-dependent Raman scattering and thermal property of CNT-based materials have been studied in our previous work.[33,34] CNTs feature strong Raman signals and provide the opportunity for validating plasmonic heating as the characterization material. In addition, the enhancement of Raman signals induced by plasmon resonance would provide a better thermal resolution of Raman thermometry, because the enhanced signal would result in lower noise in data processing. Herein, an AuNPs array is fabricated to generate the plasmonic effect and multi-walled CNTs (MWCNTs) are dispersed on top of the AuNPs array. The surface-enhanced Raman thermometry is employed to probe the local temperature and thermal transport in MWCNTs under plasmonic heating.

Results and discussion

Experimental and simulated optical enhancement

For the direct application of Raman thermometry, the AuNPs array is patterned on a silicon substrate. Template-assisted lithography based on ultrathin alumina membrane (UTAM) is employed in the fabrication of AuNPs combined with the thermal evaporation method (see Experimental section for details).[35,36] The SEM image in the inset of Fig. 1a shows that the AuNPs are arranged in a hexagonal array. The average diameter and periodicity of AuNPs are 30.2 ± 4.1 nm and 64.6 ± 2.4 nm, respectively. By comparing the Raman signal of the Si-band between AuNPs/Si and bare Si, the Raman enhancement factor of AuNPs is obtained.[2] From the experimental results (Fig. 1a), it is found that under the excitation of a 532 nm diode laser, the Raman signal of the Si-band can be enhanced by 18% when the large area of silicon is covered by AuNPs. It has been validated that the enhanced Raman scattering of patterned silicon with respect to bare silicon can be attributed to

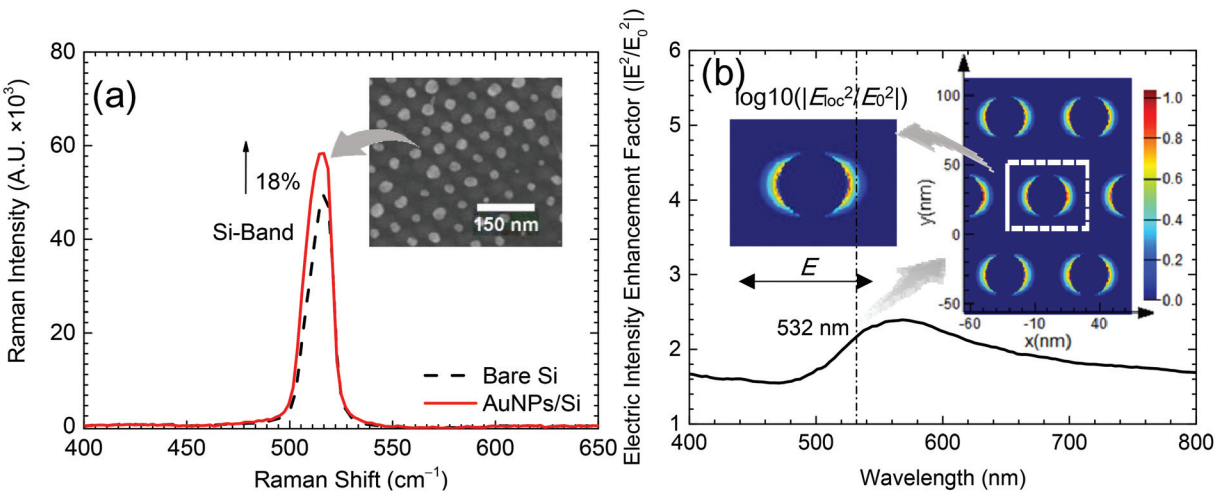

Fig. 1 (a) Raman spectra of the Si-band for AuNPs/Si and bare Si. Peak intensity of the Si-band is enhanced by 18% due to AuNPs. The inset depicts an SEM image of AuNPs array on the silicon substrate. (b) Calculated averaged electric intensity enhancement factor ($|E_{loc}^2/E_0^2|$) over the top surface of AuNPs as a function of incident wavelength. The insets depict the electric field intensity enhancement ($|E_{loc}^2/E_0^2|$, on a log scale) distribution on the top surface.

the surface plasmon property of metallic nanostructures according to Lorite *et al.*'s work[37] and our previous work.[38] The simulated extinction spectrum of AuNPs exhibits a plasmon band in the range of 400 nm to 800 nm with a peak wavelength at 554 nm and agrees well with the measured results of gold nanoparticles with similar size (see ESI section 2† for details).[39] Therefore, the plasmon property of the AuNPs could be validated in combination with the Raman enhancement measurement.

For further understanding the distribution of optical enhancement, the electromagnetic intensity around AuNPs is simulated (see Experimental section for details). The diameter and the periodicity of AuNPs are important parameters in the simulation models. The effects of their deviations on the calculated electric intensity enhancement are evaluated and they are found to be negligible (see ESI section 3† for details). The results (Fig. 1b) reveal that the AuNPs exhibit a resonant response with a peak wavelength of 560 nm. At the experimental wavelength (532 nm), the overall enhancement factor for electric intensity is 2.2. The calculated Raman enhancement factor (the second power of the electric intensity enhancement factor)[40] is 4.8. The simulation is such that 10%–50% defects in the AuNPs array may cause a reduction of 8%–44% in the Raman enhancement factor (see ESI section 3† for details). The experimental values represent averaged effects over the laser focal spot region, which is significantly larger with respect to the size of the AuNPs. Therefore, the calculated Raman enhancement factor higher than the experimental value is reasonable if the imperfection in the AuNPs array is taken into account. The simulation results (the inset of Fig. 1b) show that owing to the excitation of the plasmonic effect around AuNPs, the electric field in the vicinity of AuNPs is strongly confined within a few nanometers and distributes nonuniformly at the surface, resulting in an enhancement in the silicon Raman peak strengths.[40]

Temperature rise in MWCNTs induced by plasmonic heating

MWCNTs dispersed on a silicon substrate coated with AuNPs act as the characterization target while the bare silicon region without coating acts as the control group. For consistency in measurement, the sample (MWCNTs/AuNPs/Si) and the control group (MWCNTs/Si) are on the same silicon chip. SEM images (Fig. 2a and b) of the sample and the control group show that MWCNTs (estimated diameter from 15 to 40 nm, length: 10 μm) agglomerate and distribute randomly on the substrate due to the van der Waals forces.[41] This agglomeration results in a nonuniform thickness distribution in the MWCNT layer, and may cause experimental uncertainties in the Raman signals if treated improperly (see Experimental section for details). For comparison, the measurements need to be conducted on spots of the sample and control group with similar thicknesses of MWCNTs. Before the heating experiment, these spots are confirmed in advance. In Fig. 2c, the higher baseline of the Raman spectrum from the sample stems from the fluorescence background of the AuNPs and is subtracted in data processing.[42] It is found that the Raman spectrum of the control group includes the Si-band (520 cm^{-1}), D-band (defects and disorder of the MWCNTs structure, 1347 cm^{-1}), G-band (close to graphite mode, 1586 cm^{-1}) and 2D-band (second-order harmonic, 2700 cm^{-1}) of MWCNTs. The D-band, G-band and 2D-band of the sample show a redshift (lower than 3 cm^{-1}), with respect to the control group,[42] indicating that the charge transfer between MWCNTs and AuNPs is weak, which makes a minor contribution to the Raman enhancement.[43] Moreover, the intensity ratio of D-band to G-band (I_D/I_G) and the ratio of D-band to 2D-band (I_D/I_{2D}) are 1.19 and 4.19, respectively, close to those of the control group (1.20 and 4.14, respectively). It means that the presence of AuNPs does not cause new defects as well as structural changes in MWCNTs.[44]

The peak intensities of the D-band and G-band exhibit negligible variations from 302 K to 363 K,[45] while their peak positions shift with temperature (Fig. 3a and inset of Fig. 3b). Among the different bands of MWCNTs, the D-band has the strongest intensity and is used as the temperature indicator. Its temperature coefficient is characterized as −0.02 cm^{-1} K^{-1} (Fig. 3b) in the calibration experiment, which agrees well with the literature values (−0.017 cm^{-1} K^{-1} to −0.019 cm^{-1} K^{-1}).[45,46] In the laser heating experiment, laser with different powers is irradiated on the same spot of the sample and the control group. The peak shift of the D-band as a function of laser power is shown in Fig. 3c. As the laser intensity is increased, the D-band of MWCNTs shows a redshift for both the sample and the control group. The slope of the D peak shift to the laser power is −0.0139 cm^{-1} mW^{-1} for the sample, which is ∼3 times that of the control group (−0.0044 cm^{-1} mW^{-1}). Based on the calibration results, the temperature rise in MWCNTs under different laser powers is obtained. As shown in Fig. 3d, when the power is increased from 12 mW to 30 mW, MWCNTs in the control group show a small temperature rise (less than 6.6 ± 2.0 K). However, the temperature rise in MWCNTs in the sample is obviously higher over the same laser power range, and its maximum value is about 20.7 ± 3.6 K. The monitored MWCNTs are both from the same batch and have similar structural distributions. Considering that the laser spot is large enough, the measured heating effects are a general description of thermal transport through CNTs. The difference in temperature rise between the sample and the control group is attributed to two aspects: (1) the enhanced photon absorption generated by the plasmonic AuNPs, and (2) the lower thermophysical properties of MWCNTs on AuNPs/Si.

The temperature rise due to photon absorption enhancement can be calculated as $\Delta T_{CNTs} = s^*M^*P$, where s is the slope between temperature rise in MWCNTs in the control group and laser power (0.22 K mW^{-1}) due to the pure laser heating effect on MWCNTs (Fig. 3d), M is the photon absorption enhancement factor and P is the laser power, 30 mW. The enhanced photon absorption in MWCNTs is proportional to the electric intensity enhancement depending on its physical

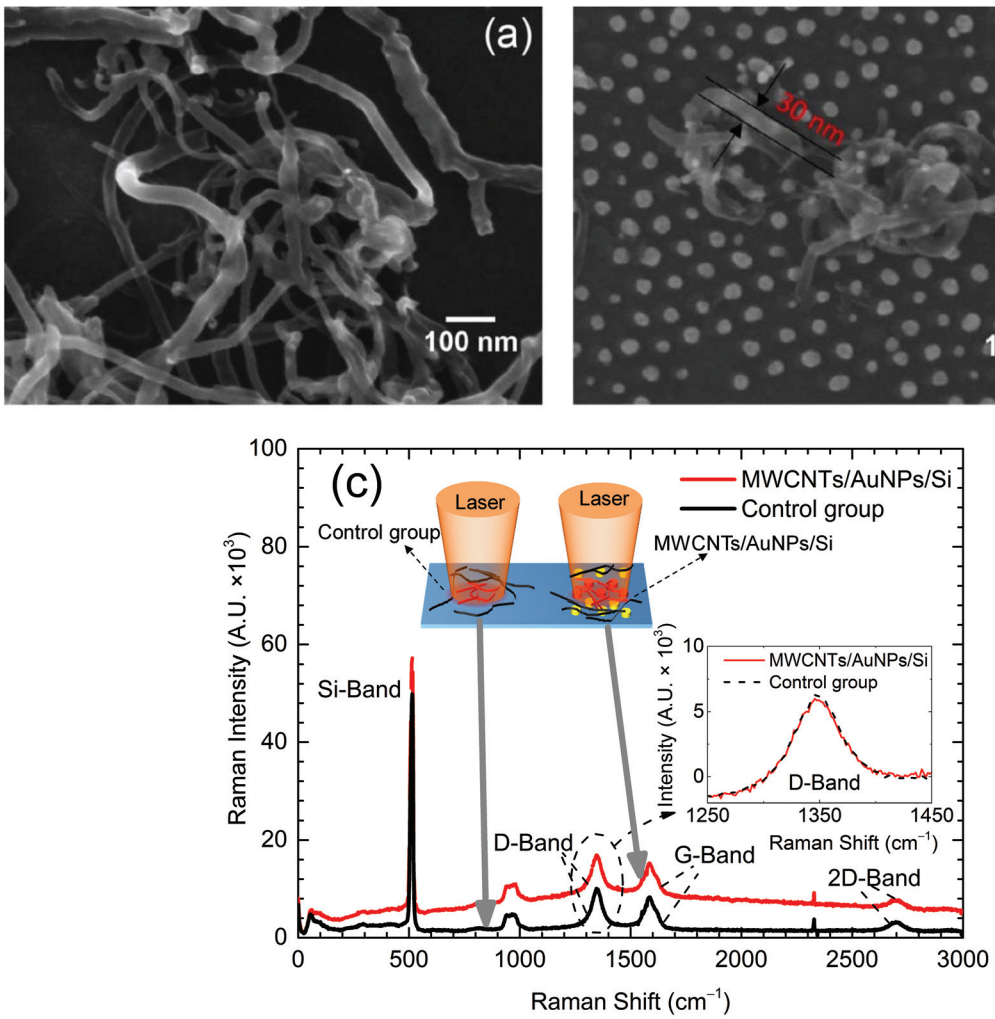

Fig. 2 SEM images of (a) MWCNTs/Si (as a control group) and (b) MWCNTs/AuNPs/Si. The diameter of an individual MWCNT ranges from 15 nm to 40 nm. (c) Comparison of Raman spectra from targeting locations between the sample and control group, with the Si-band, D-band, G-band and 2D-band of MWCNTs. The lower inset depicts that the peak intensity of the D-band for the sample is similar to that of the control group. The upper inset illustrates the schematic of laser heating in the sample and control group by adjusting laser power.

definition.[19,47] The electric intensity enhancement around MWCNTs can be estimated from Raman experiments. The Raman enhancement of MWCNTs is mainly attributed to the plasmonic AuNPs, and has been confirmed in Bäuml *et al.*'s work on polarized surface-enhanced Raman measurements of suspended CNTs on Pt–Re nanoantennas.[48] As shown by the Raman enhancement of our AuNPs array (Fig. 1a), the average electric intensity enhancement is around 1.09 (the square root of Raman enhancement 1.18).[40] ΔT_{CNTs} is calculated as 7.2 K. If we use the value of simulated electric intensity enhancement factor (~2.2), the corresponding temperature rise is 14.5 K, which is the upper limit since the factor is from a perfect pattern without defects. The temperature rise due to the absorption enhancement (7.2 K–14.5 K) is smaller than the AuNPs-assisted heating effect (20.7 K), indicating that photon absorption enhancement is partially responsible for the difference in temperature rise of MWCNTS between the sample and the control group.

Minimized heating effects on AuNPs and Si substrate

Before analyzing thermal transport in MWCNTs and exploring the thermophysical properties of MWCNTs, the laser heating effects on AuNPs and Si substrate should be studied. The heat generation in AuNPs *via* the plasmon decay is expressed by the enhanced light absorption,[6] providing a way to analyze the theoretical temperature rise in AuNP arrays. The thermal transport around AuNPs (if any) is complex considering the thermal contact with the silicon substrate and surrounding air. Herein, we roughly estimate the value based on a theoretical model proposed by Baffou *et al.*[19] The model is for a periodic array of plasmonic NPs located at the interface between two homogeneous media to simplify the reported numerical method,[15] and has been validated by temperature measurements on AuNPs. In this model, the temperature rise (ΔT) in an AuNP is expressed by $\Delta T = \Delta T_s + \Delta T_{ext}$, where ΔT_s represents the temperature rise confined at the vicinity of each NP due to the self-

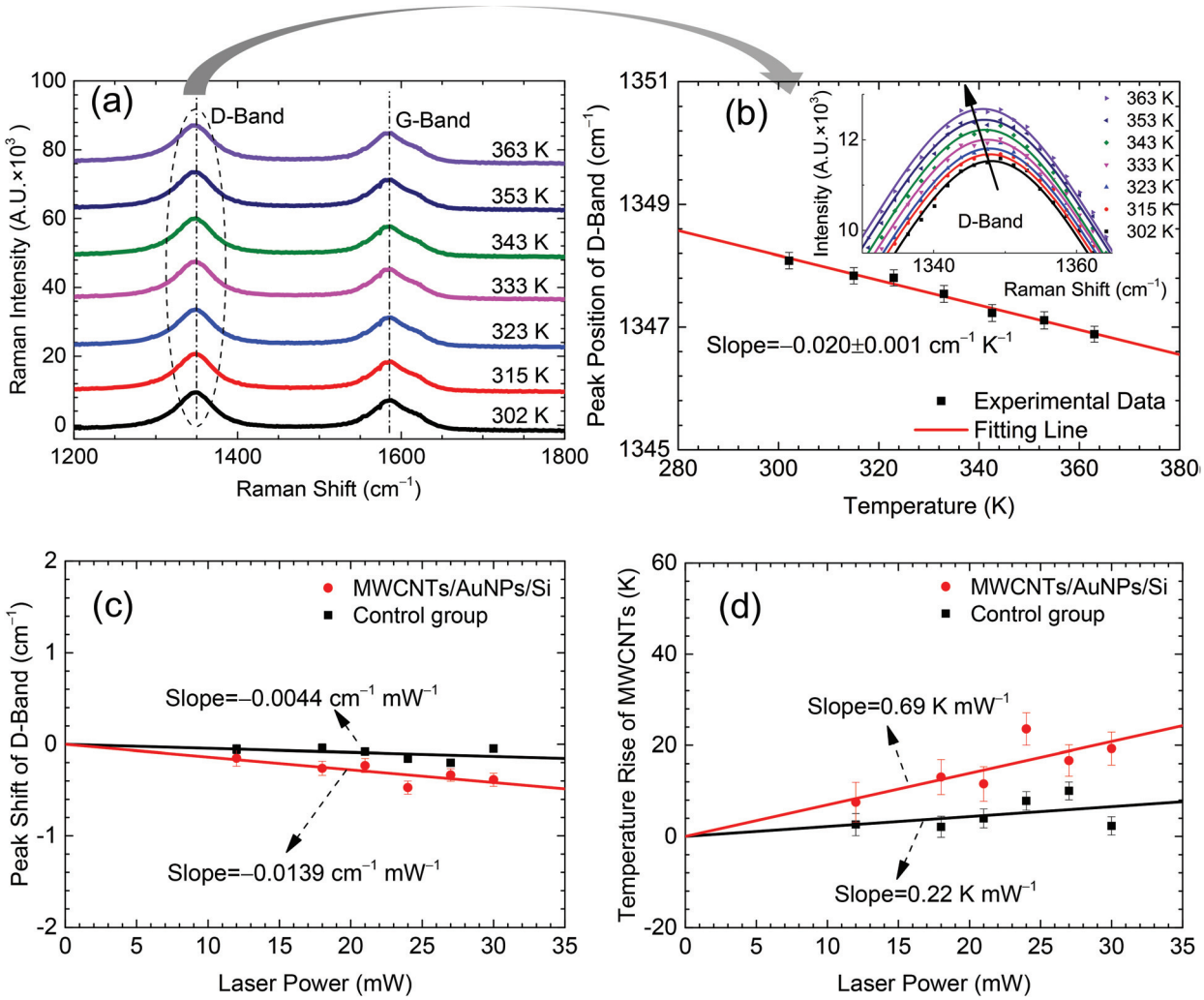

Fig. 3 (a) Raman spectrum of MWCNTs at different temperatures, with no variations in peak intensity of the D-band and G-band but variations in the peak positions of the D-band and G-band. (b) The D-band peak position as a function of temperature. The inset depicts that the fitting line of the D-band spectrum downshifts as temperature is increased from 302 K to 363 K. (c) The D-band peak shift of the sample shows linearity with laser power, with slope three times as large as that of the control group. (d) Temperature rise in MWCNTs in the sample deduced based on the results in (a–c), higher than that in the control group at the same laser power.

heating and ΔT_{ext} represents the smooth temperature profile throughout the array due to the accumulated effect from neighboring AuNPs.

ΔT_s is given by $\Delta T_s = q_{Au}(4\pi\bar{k}R)^{-1}$, where $\bar{k} = 0.5(k + k_s)$ is the mean thermal conductivity of the media in the vicinity of AuNPs. k is the thermal conductivity of silicon (148 W (m K)$^{-1}$) and k_s = 0.026 W (m K)$^{-1}$ for air. The utilized mean thermal conductivity is 74.013 W (m K)$^{-1}$. R is the equivalent radius of AuNP.[15] q_{Au} is the absorbed power in an AuNP, obtained by integration of simulated power absorption per unit volume ($\dot{q}_{Au}$) (see ESI section 1† for details). The results of $\dot{q}_{Au}$ (Fig. 4a–c) indicate that its magnitude is almost uniform throughout the whole NP, with a mean value of ~1.25×10^{14} W m^{-3}. Based on the calculated q_{Au} (1.76×10^{-9} W), ΔT_s in an AuNP is estimated as 1.3×10^{-4} K, which means that the self-heating in AuNP is negligible. ΔT_{ext} is expressed by $\Delta T_{ext} \approx q_{Au}D(1 - 2A^{0.5}\pi^{-0.5}D^{-1})(4\bar{k}A)^{-1}$, where D is the diameter of the laser focal spot (50 μm), and A is the effective area of one unit-cell periodicity given by $A = \sqrt{3}p^2/2$ and p is the value of one periodicity (65 nm). The value of ΔT_{ext} is calculated as 0.1 K. The heating effect accumulated from adjacent AuNPs could be assumed negligible.

In order to evaluate the laser heating effect on the silicon substrate, Raman measurements are performed on the silicon substrate in the sample and the control group regions from 12 mW to 30 mW. Each spectrum is collected at least five times for averaging. The variations of Raman frequency shift with laser power are shown in Fig. 4d. The temperature coefficient of the Si-band is determined by Raman calibration over a temperature range from 294 K to 364 K (see ESI section 4† for details), which is fitted as −0.023 cm^{-1} K^{-1}, agreeing well with the reported values (−0.0201 cm^{-1} K^{-1} to −0.0247 cm^{-1} K^{-1}).[49–51] Fig. 4d shows that the Raman peak shift of the Si-band does not significantly vary with the laser power. The

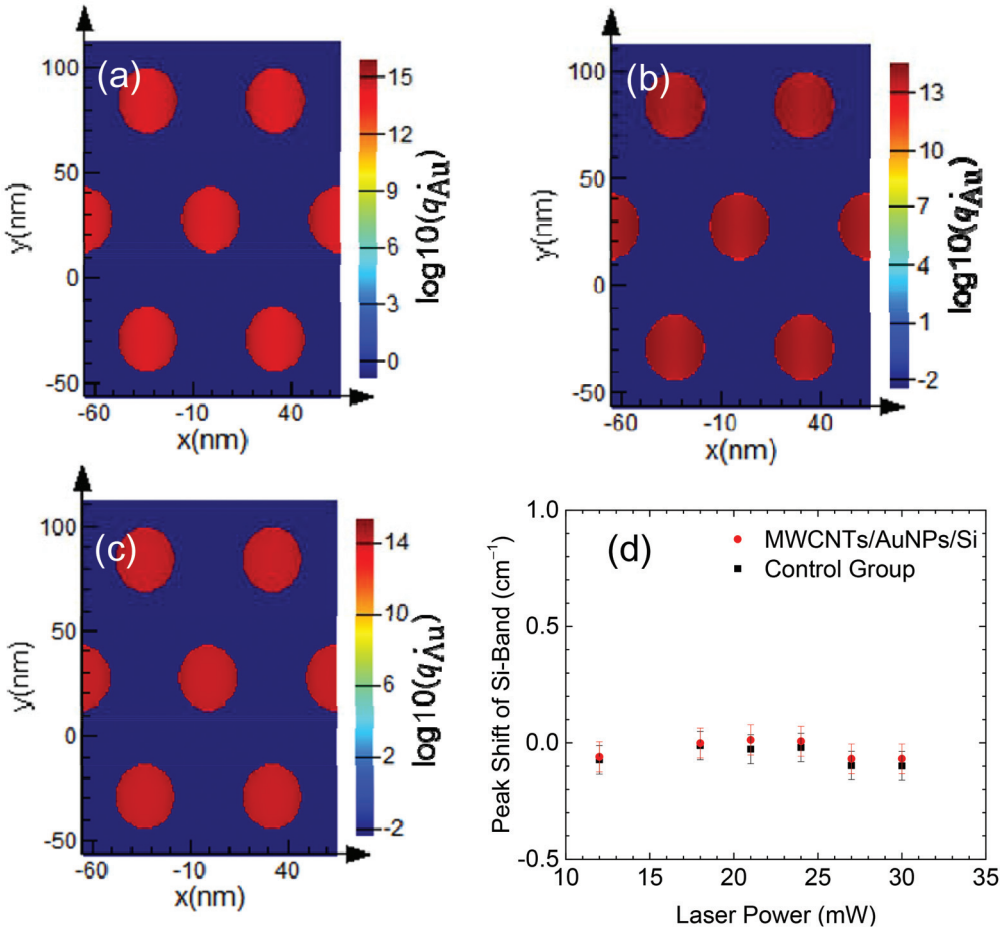

Fig. 4 The distribution of power absorption per unit volume (on a log scale) on three *xy* planes including (a) bottom, (b) center and (c) top surface. The average value is ~1.25 × 10^{14} W m^{-3} under incident laser intensity of 0.015 mW μm^{-2}. (d) Peak shift of the Si-band under different laser powers for the sample and control group.

temperature rises in the silicon substrate for the sample and the control group are both below 1.3 K, which are negligible. The maximum laser intensity used here is 0.015 mW μm^{-2}, two orders of magnitude lower than the threshold value (2.5 mW μm^{-2}) for producing observable temperature rise in bulk silicon.[52] Thereby, the temperature rise in the AuNPs and silicon substrate is negligible. Meanwhile, we could deduce that the AuNPs and silicon substrate can act as perfect heat sinks for MWCNTs which contact either the AuNPs or silicon substrate.

Thermal transport in MWCNTs

The SEM image of MWCNTs (Fig. 2b) shows that there are a large number of contact points in the MWCNT agglomerates. Thermal transport across these MWCNT junctions plays a critical role in the collective heat transfer through MWCNT agglomeration,[53–55] which is determined by various geometrical,[56] structural[57] and external parameters[58] and is extremely complicated. In order to analyze and compare the thermal property of MWCNTs between the sample and the control group, a generalized model is used to describe the complex heat transfer through MWCNTs. Under the compensative effect of various internal and external factors, agglomerated MWCNTs is regarded as a one-dimensional MWCNT composite. The temperature rise measured by Raman thermometry is regarded as the average temperature rise in this one-dimensional substitute. In practice, to support the material, the ends of such composite are always in thermal contact with the silicon substrate or AuNPs. The temperature rise in the AuNPs and the silicon substrate is evaluated to be negligible. Therefore, the temperature at the ends of the composite is room temperature. The heat generated inside the one-dimensional composite is transferred along the axial direction, as shown in Fig. 5a and b. Therefore, the one-dimensional steady-state model is applicable.

The mean temperature of the MWCNT composite is evaluated by:[34] $\bar{T} = \overline{\dot{q}_C} L^2 (3k_C)^{-1} + T_0$, where $(\bar{T} - T_0)$ is the mean temperature rise, directly obtained from the experimental results in Fig. 3d, L is the half length of MWCNT (5 μm), k_C is the thermal conductivity of MWCNT, and $\overline{\dot{q}_C}$ is the mean heat generation per unit volume deduced from the photon absorption in MWCNTs, which is estimated by

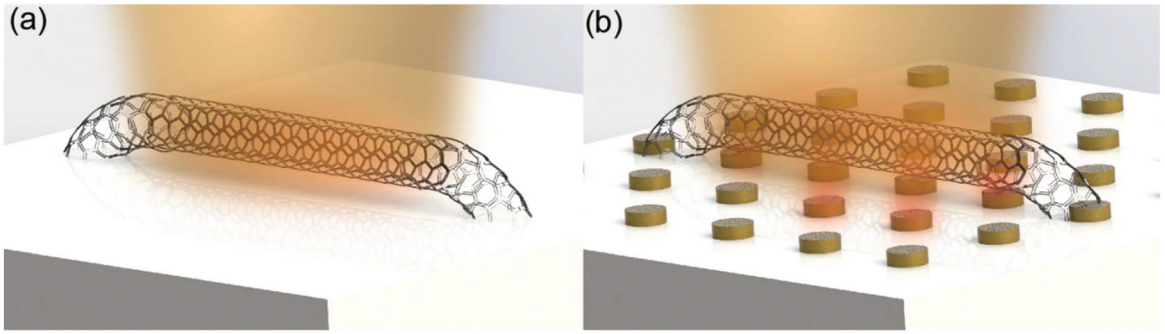

Fig. 5 The schematic of thermal transport in a single MWCNT on a silicon substrate (a) without and (b) with AuNPs along the axial direction under the irradiation of a laser beam.

$\overline{\dot{q}_C} = P_0 \alpha M r_t r_0^{-2} A_C^{-1}$, where P_0 (30 mW) is the laser energy, r_t (15 nm) is the radius of MWCNT, measured from Fig. 2b, A_C is the cross section area, r_0 is the radius of the laser focal spot, M is the mean electric field intensity enhancement factor (1.09 for near field enhancement of AuNPs, and 1 for bare silicon), and α is the laser absorptance: 0.037, estimated based on the reported values for the MWCNTs with similar structure and incident wavelength.[59] The equivalent thermal conductivity of MWCNT is calculated by solving the above equation as 47 W (m K)$^{-1}$ for the one on bare silicon (control group) and 16 W (m K)$^{-1}$ for the one on AuNPs/Si. They are apparent values. Since the thermal resistance of numerous CNT junctions and the value of the calculated thermal conductivity are both small and much lower than that of a single suspended MWCNT.[60]

Compared with the control group, the equivalent thermal conductivity of MWCNTs on AuNPs is suppressed by 66%, though the MWCNT sample is from the same batch and all the other experimental conditions are the same. To explore the origin, the mean free path of phonons in MWCNTs is roughly estimated by $l \approx k_C(C_V v)^{-1}$ based on the kinetic theory.[61] Assuming C_V as 629.8 kJ (m^3 K)$^{-1}$ and v the sound velocity of MWCNTs as 10^4 m s^{-1}, the phonon mean free path of the control group is estimated to be 7 nm. The length dimension of the region confining the electromagnetic field is about 6 nm along the x axis and 28 nm along the y axis, as shown in the inset of Fig. 1b. The size of the hot spots is just comparable to the calculated mean free paths of phonons. Therefore, the localized thermal transport may become quasi-ballistic which would greatly reduce the thermal conductivity of MWCNTs.[62] Additionally, as shown in the inset of Fig. 1b, the hot spots distribute nonuniformly across the layer of AuNPs, leading to a nonuniform heating on MWCNTs and thus resulting in nonequilibrium in phonon transport from randomly distributed hot spots and also causing a reduction in thermal conductivity of MWCNTs, which is another reason for the higher temperature rise observed in the sample. The current study is conducted at low laser energy levels; a more significant temperature difference could be observed if the AuNPs are exposed to a much more intense laser energy below 31.4 W on the premise that the AuNPs would not be damaged.[63]

Conclusions

We have characterized the plasmonic heating effect of a two-dimensional array of AuNPs on MWCNTs and found that the temperature rise in MWCNTs under plasmonic heating is about two times higher than that in the same materials on bare silicon under the same levels of laser energy irradiation. The large difference in temperature rise is partially attributed to the enhanced photon absorption of MWCNTs as validated by the enhanced Raman signal due to the plasmon resonances of AuNPs. In addition, the nanoscale hot spots at the top surface of the AuNPs result in the quasi-ballistic phonon transport inside MWCNTs, and the reduction of phonon mean free path lowers the thermal conductivity of MWCNTs. This work offers a feasible way for thermal characterization in near field based on the Raman thermometry. Meanwhile, our results are beneficial for understanding the near-field heating effect as well as the quasi-ballistic thermal transport in low-dimensional materials.

Experimental section

Fabrication of AuNPs array

The array of AuNPs is fabricated through template-assisted lithography based on ultrathin alumina membrane (UTAM), which has been demonstrated to be an effective way for patterning well-defined NPs. The template is a 200 nm-thick commercialized UTAM that has self-organized honeycomb-like nanopores with an average diameter of 45 nm and a periodicity of 65 nm. The UTAM layer is supported by a layer of polymethyl methacrylate (PMMA). The sample fabrication processes are illustrated in Fig. 6. PMMA/UTAM is first transferred to a silicon substrate [(100), p-type doping]. Then, the cover is removed by acetone baths, leaving only UTAM on silicon. By using thermal evaporation, 20 nm of Au (99.99%) film is deposited on UTAM/Si with a 5 nm adhesion layer of Cr (99.99%), under high vacuum (2.7×10^{-4} Pa–2.8×10^{-4} Pa) with an evaporation rate of 0.03 nm s^{-1}–0.08 nm s^{-1}. After lift-off, the AuNPs array is patterned on a silicon substrate (hereafter AuNPs/Si). The plasmon-induced enhancement is con-

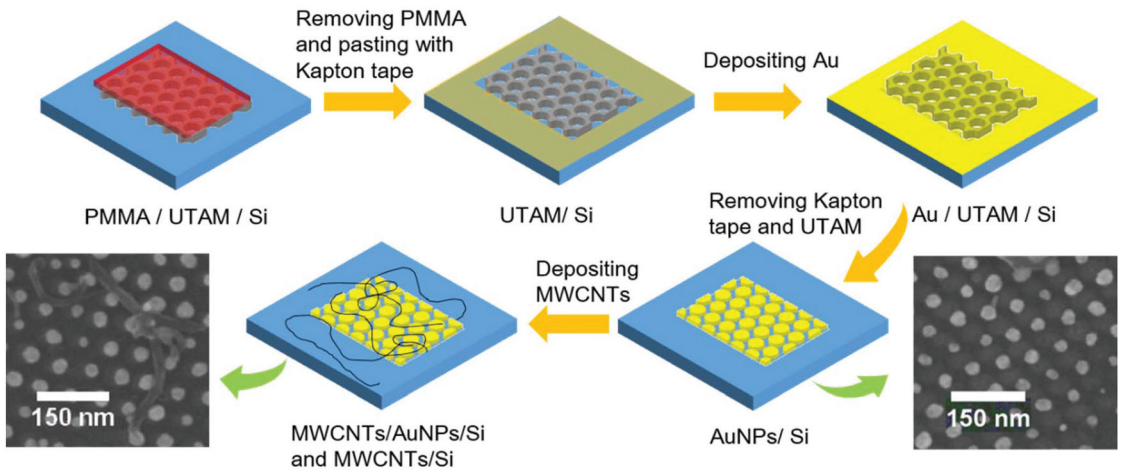

Fig. 6 The preparation processes of MWCNTs/AuNPs/Si and control group. PMMA/UTAM is carefully placed on a silicon wafer. PMMA/UTAM/Si is subsequently processed with acetone baths to remove PMMA, leaving only UTAM on the silicon as a mask. The rest of the silicon substrate is covered with Kapton tape. Gold thin film is subsequently deposited on UTAM/Si by thermal evaporation. After the Kapton tape is removed, the sample is placed in a sodium hydroxide solution for lift-off, leaving only AuNPs on the substrate, as shown in the right SEM inset. The dissolved MWCNTs are dribbled on silicon with and without AuNPs, as shown in the left SEM inset.

firmed by Raman characterization of AuNPs/Si and bare Si under the excitation of a 532 nm diode laser.

Simulation

Electromagnetic field distribution around the AuNPs array is simulated by using the finite-difference time-domain (FDTD) method.[64] The details of the simulation can be found in the ESI section 1.† The electric intensity enhancement factor is calculated by averaging the second power of field enhancement, which is represented as the ratio of the local electric field (E_{loc}) to the incident electric field (E_0, 1 V m^{-1}). The numerical model for calculating the power absorption per unit volume in AuNPs is the same as that described in the ESI section 1.† The input incident electric field is corresponding to the used laser intensity of 0.015 mW μm^{-2}.

Fabrication of MWCNTs/AuNPs/Si and MWCNTs/Si

MWCNTs are dispersed in ethyl alcohol and treated by ultrasonication for 20 minutes, before being deposited on a silicon substrate that is partially coated with AuNPs, as shown in Fig. 6. MWCNTs/AuNPs/Si and MWCNTs/Si are characterized by using a scanning electronic microscope and Raman spectrometer with a 532 nm diode laser.

Measurement setup

The schematic of the laser heating experiment is illustrated in the upper inset of Fig. 2c. For the MWCNTs/AuNPs/Si sample, the plasmonic effect of AuNPs provides additional heating in MWCNTs besides the direct laser heating. As a comparison, only direct laser heating is involved in the control group. To eliminate the error caused by single data, the temperature rise in MWCNTs is estimated by the fitted slope between laser power and D-band peak shift. A Raman spectrometer (B&W Tek) equipped with a 532 nm diode laser (energy adjustable) is used for exciting and collecting Raman signals and heating samples. The laser focal spot is 50 μm in diameter, and the samples are illuminated by laser power from 12 mW to 30 mW, which generates power intensities ranging from 0.006 mW μm^{-2} to 0.015 mW μm^{-2}. The integration time varies from 1.5 minutes to 4 minutes to get strong Raman signals. To ensure the accuracy of the measurements, each spectrum is collected at least five times for averaging. The peak position of the D-band and Si-band are obtained by Lorentz function fitting. The locations with similar MWCNT thickness on the AuNPs/Si samples and the control group are firstly confirmed (see ESI section 4† for details). Since it is difficult to directly measure the MWCNT thickness, we use the Raman intensity of the D-band to monitor the MWCNT thickness variation.[65] The D-band peak intensity of the sample correlates closely with both MWCNT thickness and Raman enhancement. By using Raman mapping (scanning), the regions with the smallest difference in the D-band intensity (or silicon intensity) for the sample and the control group are labeled, as shown in Fig. 2c. The signals are recorded at an integration time of 1.5 minutes under the same focal levels. The lower inset of Fig. 2c shows that, between the MWCNTs/AuNPs/Si sample and the control group, the D-band intensity differs by 5%. Considering the optical enhancement generated by AuNPs, the MWCNTs at these two locations are considered with the same thickness.

Conflicts of interest

The authors declare that they have no conflict of interest.

Acknowledgements

Y. Y. thanks the financial support from the National Natural Science Foundation of China (No. 51576145).

X. Z., A. L. and X. Z. acknowledge the National Science Foundation (CMMI-1762739 and ECCS-1810252).

Notes and references

1 J. Kneipp, H. Kneipp and K. Kneipp, *Chem. Soc. Rev.*, 2008, **37**, 1052–1060.
2 P. Kusch, S. Mastel, N. S. Mueller, N. Morquillas Azpiazu, S. Heeg, R. Gorbachev, F. Schedin, U. Hübner, J. I. Pascual, S. Reich and R. Hillenbrand, *Nano Lett.*, 2017, **17**, 2667–2673.
3 Y. Shen, X. Cheng, G. Li, Q. Zhu, Z. Chi, J. Wang and C. Jin, *Nanoscale Horiz.*, 2016, **1**, 290–297.
4 J. C. Ndukaife, V. M. Shalaev and A. Boltasseva, *Science*, 2016, **351**, 334–335.
5 N. Zhou, X. Xu, A. T. Hammack, B. C. Stipe, K. Gao, W. Scholz and E. C. Gage, *Nanophotonics*, 2014, **3**, 141–155.
6 K. Setoura, S. Ito and H. Miyasaka, *Nanoscale*, 2017, **9**, 719–730.
7 C. Ma, J. Yan, Y. Huang, C. Wang and G. Yang, *Sci. Adv.*, 2018, **4**, eaas9894.
8 J. Yan, P. Liu, C. Ma, Z. Lin and G. Yang, *Nanoscale*, 2016, **8**, 8826–8838.
9 B. C. Marin, J. Ramírez, S. E. Root, E. Aklile and D. J. Lipomi, *Nanoscale Horiz.*, 2017, **2**, 311–318.
10 P. Christopher, H. Xin and S. Linic, *Nat. Chem.*, 2011, **3**, 467–472.
11 Y. Osaka, S. Sugano and S. Hashimoto, *Nanoscale*, 2016, **8**, 18187–18196.
12 G. Baffou and R. Quidant, *Laser Photonics Rev.*, 2012, **7**, 171–187.
13 A. O. Govorov and H. H. Richardson, *Nano Today*, 2007, **2**, 30–38.
14 O. Blum and N. T. Shaked, *Light: Sci. Appl.*, 2015, **4**, e322.
15 G. Baffou, R. Quidant and F. J. García de Abajo, *ACS Nano*, 2010, **4**, 709–716.
16 R. Rodríguez-Oliveros and J. A. Sánchez-Gil, *Opt. Express*, 2012, **20**, 621–626.
17 P. Zolotavin, A. Alabastri, P. Nordlander and D. Natelson, *ACS Nano*, 2016, **10**, 6972–6979.
18 A. Lalisse, G. Tessier, J. Plain and G. Baffou, *Sci. Rep.*, 2016, **6**, 38647.
19 G. Baffou, P. Berto, E. Bermúdez Ureña, R. Quidant, S. Monneret, J. Polleux and H. Rigneault, *ACS Nano*, 2013, **7**, 6478–6488.
20 Z. J. Coppens, W. Li, D. G. Walker and J. G. Valentine, *Nano Lett.*, 2013, **13**, 1023–1028.
21 A. Downes, D. Salter and A. Elfick, *Opt. Express*, 2006, **14**, 5216–5222.
22 W. Zhang, T. Schmid, B. S. Yeo and R. Zenobi, *J. Phys. Chem. C*, 2008, **112**, 2104–2108.
23 O. A. Yeshchenko, N. V. Kutsevol and A. P. Naumenko, *Plasmonics*, 2016, **11**, 345–350.
24 J. H. Liu, H. H. Xie, Y. D. Hu, X. Zhang and Y. Y. Zhang, *Int. J. Heat Mass Transfer*, 2017, **108**, 572–576.
25 J. Liu, T. Li, Y. Hu and X. Zhang, *Nanoscale*, 2017, **9**, 1496–1501.
26 Q. Y. Li, K. Takahashi and X. Zhang, *Int. J. Heat Mass Transfer*, 2019, **134**, 539–546.
27 Y. N. Yue, J. C. Zhang and X. W. Wang, *Small*, 2011, **7**, 3324–3333.
28 Q. Y. Li, W. G. Ma and X. Zhang, *Int. J. Heat Mass Transfer*, 2016, **95**, 956–963.
29 Q. Y. Li, K. Xia, J. Zhang, Y. Zhang, Q. Li, K. Takahashi and X. Zhang, *Nanoscale*, 2017, **9**, 10784–10793.
30 H. D. Wang, J. H. Liu, Z. Y. Guo, X. Zhang, R. F. Zhang, F. Wei and T. Y. Li, *Nanoscale Microscale Thermophys. Eng.*, 2013, **17**, 349–365.
31 L. Qiu, P. Guo, X. Yang, Y. Ouyang, Y. Feng, X. Zhang, J. Zhao, X. Zhang and Q. Li, *Carbon*, 2019, **145**, 650–657.
32 E. F. Antunes, A. O. Lobo, E. J. Corat and V. J. Trava-Airoldi, *Carbon*, 2007, **45**, 913–921.
33 Y. Yue, X. Huang and X. Wang, *Phys. Lett. A*, 2010, **374**, 4144–4151.
34 M. Li and Y. N. Yue, *J. Nanosci. Nanotechnol.*, 2015, **15**, 3004–3010.
35 A. Al-Haddad, Z. Zhan, C. Wang, S. Tarish, R. Vellacheria and Y. Lei, *ACS Nano*, 2015, **9**, 8584–8591.
36 Q. Fu, Z. Zhan, J. Dou, X. Zheng, R. Xu, M. Wu and Y. Lei, *ACS Appl. Mater. Interfaces*, 2015, **7**, 13322–13328.
37 I. Lorite, A. Serrano, A. Schwartzberg, J. Bueno and J. L. Costa-Krämer, *Thin Solid Films*, 2013, **531**, 144–146.
38 Y. Xu, Y. Wang, Y. Chen, Y. Yue and J. Jiang, *Mater. Res. Express*, 2018, **5**, 065057.
39 Z. Huang, G. Meng, B. Chen, C. Zhu, F. Han, X. Hu and X. Wang, *J. Nanosci. Nanotechnol.*, 2016, **16**, 934–938.
40 M. Moskovits, *J. Raman Spectrosc.*, 2005, **36**, 485–496.
41 A. Das, K. W. Stöckelhuber, R. Jurk, M. Saphiannikova, J. Fritzsche, H. Lorenz, M. Klüppel and G. Heinrich, *Polymer*, 2008, **49**, 5276–5283.
42 M. Scolari, A. Mews, N. Fu, A. Myalitsin, T. Assmus, K. Balasubramanian, M. Burghard and K. Kern, *J. Phys. Chem. C*, 2008, **112**, 391–396.
43 P. Corio, S. D. M. Brown, A. Marucci, M. A. Pimenta, K. Kneipp, G. Dresselhaus and M. S. Dresselhaus, *Phys. Rev. B: Condens. Matter Mater. Phys.*, 2000, **61**, 13202.
44 H. Chu, J. Wang, L. Ding, D. Yuan, Y. Zhang, J. Liu and Y. Li, *J. Am. Chem. Soc.*, 2009, **131**, 14310–14316.
45 S. Osswald, M. Havel and Y. Gogotsi, *J. Raman Spectrosc.*, 2007, **38**, 728–736.
46 F. Huang, K. T. Yue, P. Tan, S. L. Zhang, Z. Shi, X. Zhou and Z. Gu, *J. Appl. Phys.*, 1998, **84**, 4022–4024.
47 A. A. Balandin, S. Ghosh, W. Bao, I. Calizo, D. Teweldebrhan, F. Miao and C. N. Lau, *Nano Lett.*, 2008, **8**, 902–907.
48 C. Bäuml, T. Korn, C. Lange, C. Schüller, C. Strunk and N. Paradiso, *Phys. Rev. B*, 2017, **96**, 035408.
49 J. Menéndez and M. Cardona, *Phys. Rev. B: Condens. Matter Mater. Phys.*, 1984, **29**, 2051–2059.
50 H. H. Burke and I. P. Herman, *Phys. Rev. B: Condens. Matter Mater. Phys.*, 1993, **48**, 15016–15024.

51 X. Tang, S. Xu, J. Zhang and X. Wang, *ACS Appl. Mater. Interfaces*, 2014, **6**, 2809.
52 T. T. Rantala and J. Levoska, *J. Appl. Phys.*, 1989, **65**, 4475–4479.
53 V. Varshney, J. Lee, D. Li, J. S. Brown, B. L. Farmer, A. A. Voevodin and A. K. Roy, *Carbon*, 2017, **114**, 15–22.
54 Y. Yue, J. Zhang, Y. Xie, W. Chen and X. Wang, *Int. J. Heat Mass Transfer*, 2017, **110**, 827–844.
55 Q. Y. Li, K. Katakami, T. Ikuta, M. Kohno, X. Zhang and K. Takahashi, *Carbon*, 2019, **141**, 92–98.
56 Q. Rong, C. Shao and H. Bao, *J. Appl. Phys.*, 2017, **121**, 054302.
57 R. N. Salaway and L. V. Zhigilei, *Phys. Rev. B*, 2016, **94**, 014308.
58 W. Chen, J. Zhang and Y. Yue, *Int. J. Heat Mass Transfer*, 2016, **103**, 1058–1064.
59 Q. Y. Li, J. H. Liu, H. D. Wang, X. Zhang and K. Takahashi, *Rev. Sci. Instrum.*, 2013, **84**, 104905.
60 P. Kim, L. Shi, A. Majumdar and P. L. McEuen, *Phys. Rev. Lett.*, 2001, **87**, 215502.
61 D. J. Yang, Q. Zhang, G. Chen, S. F. Yoon, J. Ahn, S. G. Wang, Q. Zhou, Q. Wang and J. Q. Li, *Phys. Rev. B: Condens. Matter Mater. Phys.*, 2002, **66**, 165440.
62 T. Oyake, M. Sakata and J. Shiomi, *Appl. Phys. Lett.*, 2015, **106**, 073102.
63 K. Setoura, Y. Okada and S. Hashimoto, *Phys. Chem. Chem. Phys.*, 2014, **16**, 26938–26945.
64 A. Heltzel, S. Theppakuttai, S. C. Chen and J. R. Howell, *Nanotechnology*, 2008, **19**, 025305.
65 A. Duzynska, M. Swiniarski, A. Wroblewska, A. Lapinska, K. Zeranska, J. Judek and M. Zdrojek, *Carbon*, 2016, **105**, 377–386.